

Data Repository: Non-equilibrium degassing, regassing, and vapor fluxing in magmatic feeder systems

J.M. Watkins^{*1}, J.E. Gardner², K.S. Befus³

November 29, 2016

DR1 Samples

DR1.1 Sample preparation and measurements

Obsidian chips were mounted in Buehler EpoKwick™ epoxy and then ground with 400 grit silicon carbide paper to expose the sample surface. The surface was polished using progressively finer grit silicon carbide paper in the sequence 800 - 1500 - 2000 - 2500 - 3000 grit followed by 3 μm and 0.25 μm diamond paste. The polished sample was mounted on a glass slide using Crystalbond™ and sectioned to a thickness of about 1 mm using a diamond wafer saw. The sample was then ground to a thickness between 300 - 500 μm using 400 grit silicon carbide paper and the polishing procedure was repeated. Doubly-polished wafers were transferred to an aluminum sample holder for analysis by transmission Fourier Transform Infrared (FTIR) spectroscopy.

Area maps of OH, $\text{H}_2\text{O}_\text{m}$, total H_2O , and CO_2 concentrations were made using a Thermo Nicolet Nexus 670 Fourier transform infrared (FTIR) spectrometer at the University of Oregon. Conversion of a measured absorbance to H_2O or CO_2 concentration is based on the Beer-Lambert law:

$$C_i = \frac{M_i A}{\rho d \epsilon_i}, \quad (\text{DR1})$$

where M_i is the molecular weight (g mol^{-1}), A is the absorbance (peak height minus linear baseline), ρ is the sample density ($\approx 2300 \text{ g/L}$ for rhyolite glass), d is the thickness of the wafer (cm), and ϵ_i is the molar absorption coefficient (L cm mol^{-1}). We assume glass density is constant even though it may vary by up to 5% due to variations in volatile concentration among and within clasts (Newman et al., 1986). The presence of other textures may also affect glass density for a given spot analysis. We used molar absorption coefficients for OH and $\text{H}_2\text{O}_\text{m}$ from Zhang et al. (1997) and CO_2 from Behrens et al. (2004). The thickness of the wafer was measured in several spots using a digital caliper with 0.001 mm precision while the sample was still affixed to the glass slide during sample preparation. The measured thicknesses vary by less than 5% across individual clasts and we find no evidence of systematic variation (sample wedging) in the H_2O and CO_2 concentration maps.

All measurements were made using a $15\times$ objective, infrared source, MCT-A detector and KBr beamsplitter. The run settings for most area maps were as follows: $100 \mu\text{m} \times 100 \mu\text{m}$ aperture, step size of $100 \mu\text{m}$, spectral resolution of 4 cm^{-1} , 32 scans per spot, and 64 scans for the background, which was collected every 10 minutes. Example spectra from the three area maps presented in Figure 2 of the main text are shown in Fig. DR1.

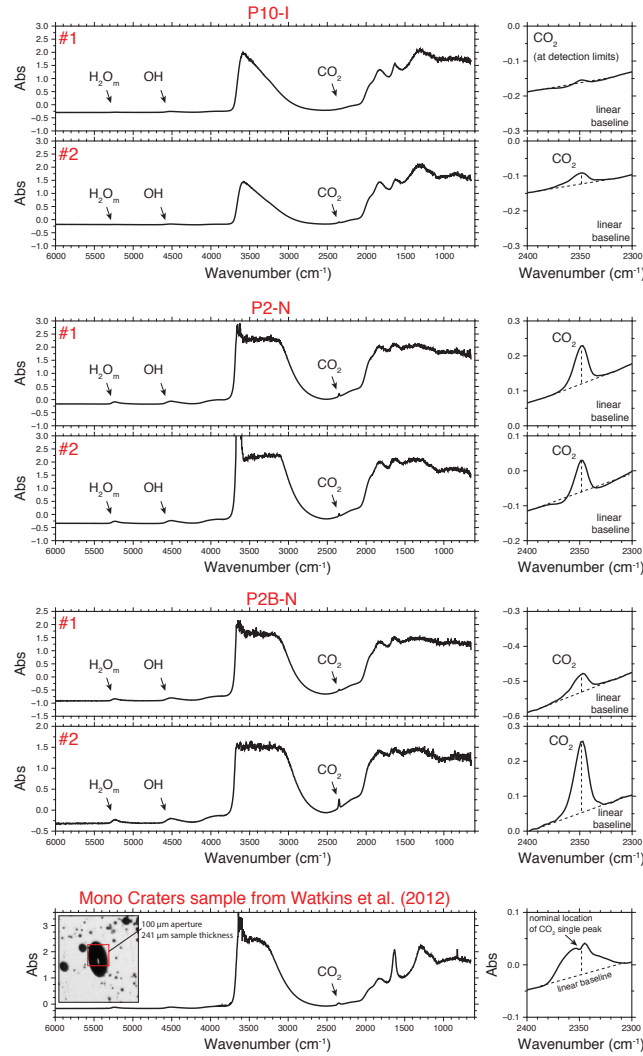


Figure DR1: Example FTIR spectra from samples with low CO₂ (P10-I), moderate CO₂ (P2-N) and high CO₂ (P2B-N). Locations of each spot analysis are shown by the black squares in Figure 2 of the main text. The single peak at 2350 cm⁻¹ is interpreted to represent dissolved CO₂. For comparison, the bottom panel shows an example spot analysis from a Mono Craters pyroclast where there is direct evidence for gaseous CO₂ in a large vapor bubble contributing to the CO₂ peak, as indicated by a double peak at 2350 cm⁻¹.

DR1.2 Data smoothing

Area maps were processed using Generic Mapping Tools (GMT) software (Wessel et al., 2013). The step size for most maps is $100 \mu\text{m}$ and the aperture size is $100 \mu\text{m} \times \mu\text{m}$. To make smoothed area maps, we make a subgrid with $10 \mu\text{m}$ spacing and interpolate the values between the measured spots. The figure below shows the area maps without smoothing, where the pixel size represents the aperture size.

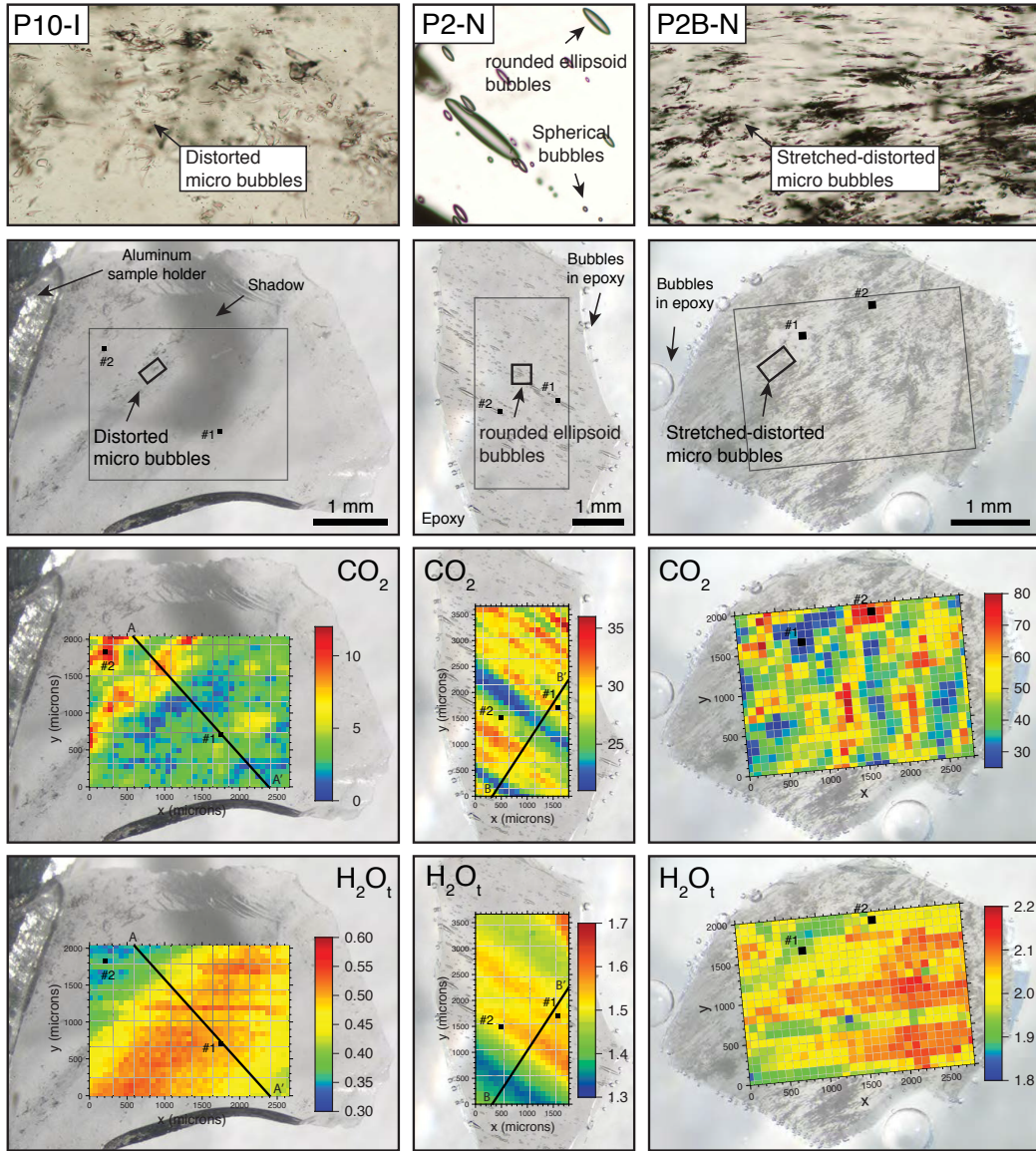


Figure DR2: Unsmoothed version of Fig 2 from the main text.

DR1.3 Absorbance to concentration conversion

A concern is that absorbance measurements may be affected by textures such as bubbles, microlites, and other particles within the glass, which may scatter the infrared light, modify the glass density, modify the molar absorption coefficient, or change the effective thickness of the glass (von Aulock et al., 2014). The key observations/interpretations that need to withstand the potential issues that can arise from textural heterogeneity within the clasts are: (1) H_2O_t and CO_2 concentrations are heterogeneous in the glass, (2) H_2O_t heterogeneities are more diffuse than CO_2 heterogeneities, and (3) the association of elevated CO_2 with distorted vesicles is evidence for CO_2 -rich vapor fluxing.

Here we scrutinize the three samples presented in Figure 2 of the main text, and in particular, the influence of bubbles on the absorbance-to-concentration conversion. First, consider sample P2-N, which has the largest bubbles of any sample we analyzed. This particular sample is $550\ \mu m$ thick, and hence the largest bubbles with diameter $\sim 50\ \mu m$ in the dimension parallel to the infrared beam only occupy about 10% at most of the analyzed volume. Figure DR3 shows a lack of 1:1 correspondence between the large bubbles and volatile concentrations. In fact, the bubble-free spots adjacent to large bubbles often yield the same volatile concentrations as the spots that directly intersect the bubbles. Furthermore, the large bubbles are isolated from one another and yet the heterogeneities in H_2O_t and CO_2 are laterally continuous across the sample, which is a clear indication that the bubbles in this sample do not significantly affect the absorbance-to-concentration conversion.

The other two samples, P10-I and P2B-N, have domains with many small, distorted or stretched-distorted bubbles in association with high CO_2 concentrations. In P2B-N, which has a higher number density of bubbles, the bubbles only occupy about 0.4 vol.% of the bulk clast, as determined from high-resolution X-ray computed tomography (Gardner et al., in revision). Even in the vesicle-rich regions of the clast, the CO_2 peaks in the spectra do not exhibit a doublet, as would be expected if gaseous CO_2 were to dominate the signal at $2350\ cm^{-1}$ (see, for example, the bottom panel in Fig. DR1). Even so, the presence of vesicles in the analyzed volume may actually lead to *underestimates* in dissolved CO_2 since gaseous CO_2 (a) lowers the average density of the glass, (b) lowers the effective thickness of the glass, and (c) exhibits a trough in the double peak at $2350\ cm^{-1}$. Although the influence of bubbles on the bulk molar absorption coefficient (ϵ) is unknown, spot analyses that intersect the large vapor bubbles in sample P2-N (as well as the bottom panel of Fig. DR1) suggest that the influence of vapor bubbles on ϵ is not dramatic. All of these issues notwithstanding, even if the elevated CO_2 in samples P10-I and P2B-N were due to CO_2 -rich gas in the vesicles, the interpretation would remain unchanged: the FTIR data from these samples constitute the first direct evidence that fluxing of a CO_2 -rich vapor through the magmatic system is contributing to the elevated CO_2/H_2O ratios (Rust et al., 2004).

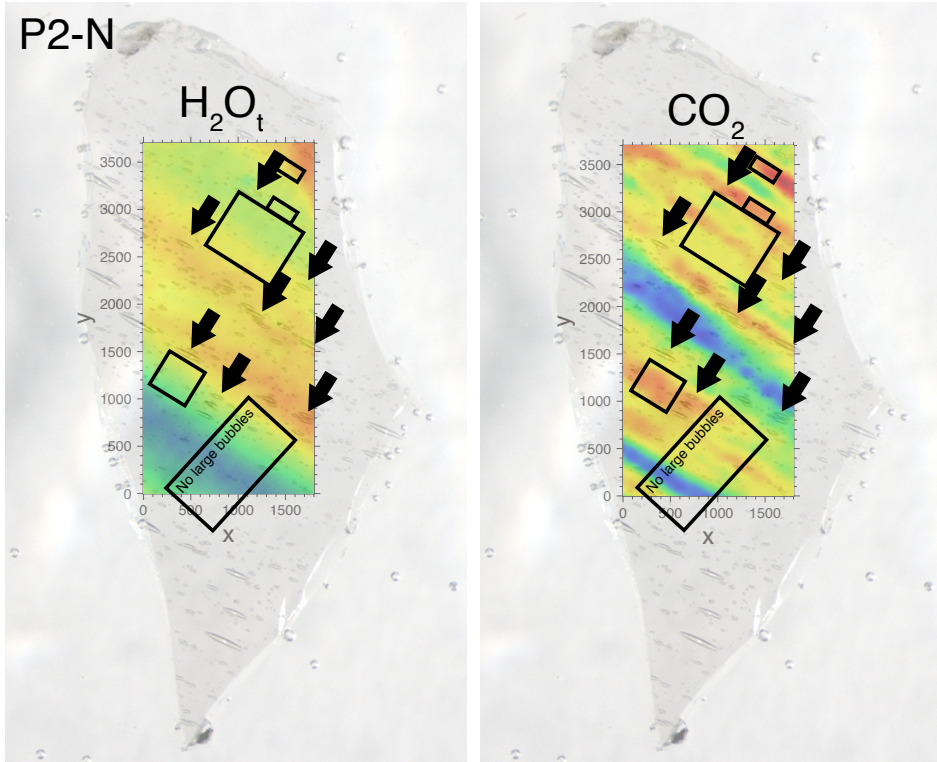


Figure DR3: A more transparent version of the area maps from sample P2N showing the lack of 1:1 correspondence between bubbles and H_2O_t or CO_2 concentration. Black arrows show the locations of large bubbles. Boxes highlight *some* of the areas with high CO_2 concentration but no large bubbles. Note that the region of the map used for diffusion modeling is also relatively free of bubbles, which justifies the model assumption of single-phase diffusion.

DR1.4 Estimating uncertainty

The textural heterogeneity within clasts makes it difficult to place quantitative error bars on any or all H₂O and CO₂ spot analyses within an area map. There are three ways in which the uncertainty is assessed. First, we can adjust the color scale on the area maps until the data appear “noisy.” This approach is shown for the relatively degassed samples P10-C and P10-E in Figure DR5. Consider sample P10-C, where based on visual inspection we conclude that the CO₂-rich band is “real” but the rest of the clast contains 3 ppm CO₂ with an uncertainty of about 3 ppm. The low-H₂O band at the top of P10-C is also “real” because it does not correlate with the CO₂ data and there are no visible textures modifying the properties of the glass in that region. This suggests an uncertainty of about 0.05 wt%. The percent relative uncertainty is much lower for samples with greater volatile contents, but it must be kept in mind that different heterogeneities affect uncertainty differently. For example, the opaque portions of clasts in Figure DR4 yield low dissolved volatile contents that are not “real” because infrared light at all wavelengths is being absorbed. Second, we screen areas of samples with low transmission or where H₂O and CO₂ are clearly influenced by textures in the same way (Figs. DR4 - DR6). In all of the samples analyzed, there is a notable lack of co-variation between CO₂ and H₂O. Hence, in most instances, bubbles and other textures are not scattering the infrared light or modifying the bulk properties of the samples in such a way that compromises the data or interpretation. Third, we perform resolutions tests by adjusting instrument settings (aperture size, scans per spot and wavenumber bin size) to further demonstrate that the relative variations in H₂O and CO₂ we report are robust (Fig. DR7).

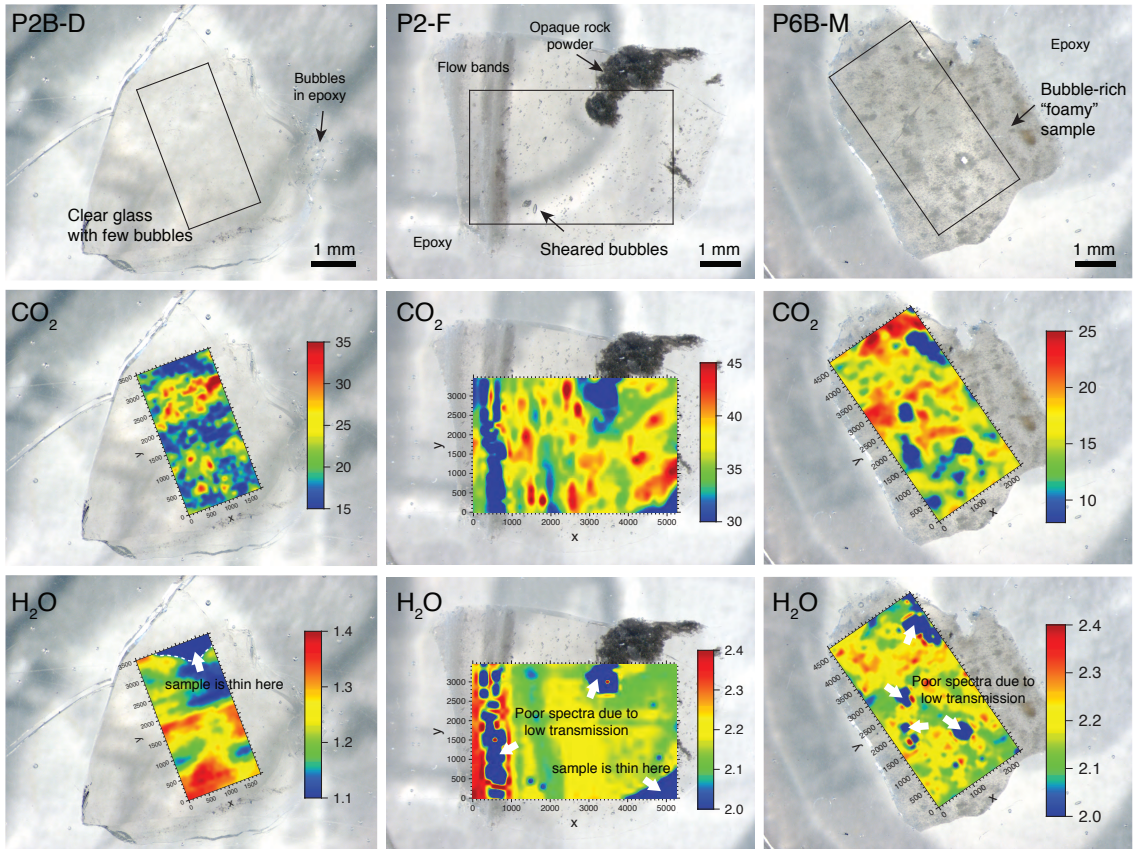


Figure DR4: Area maps of three clasts where data filtering was necessary. White arrows point to regions that have been filtered from Figure 2 of the main text due to poor spectra or thinner parts of the sample. The unfiltered version of Figure 2 is presented as Figure DR6.

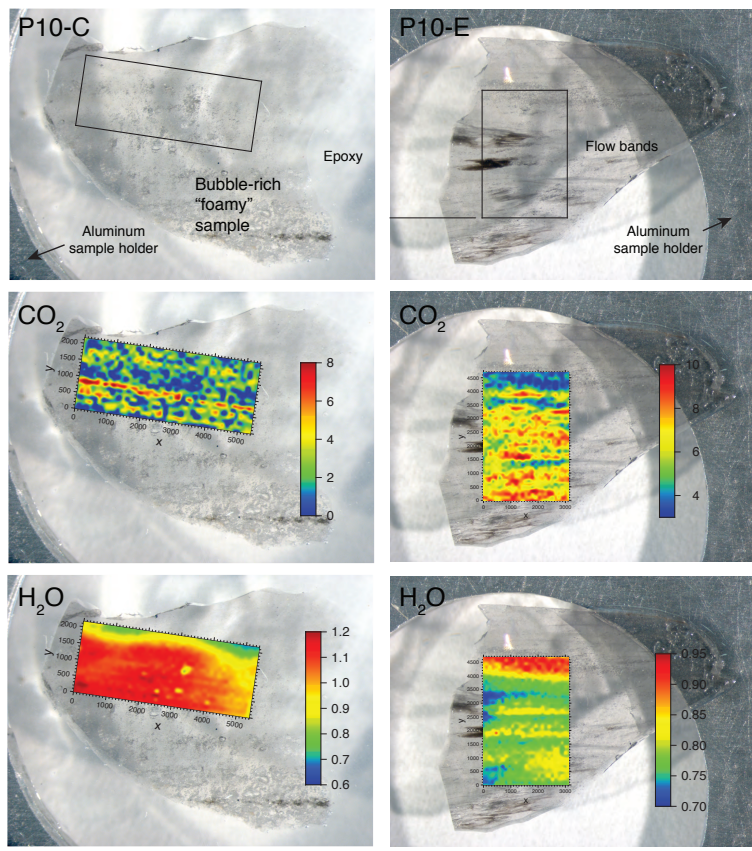


Figure DR5: Area maps of the two samples with the lowest total volatile contents. Many of the patchy variations in CO₂ are smaller than detection limits. However, the high-CO₂ band in P10-C and the low CO₂ band at the top of P10-E are likely to represent true variability. Note that the variations in H₂O in both samples are not due to sample wedging because they similar variations are not observed in the CO₂ data.

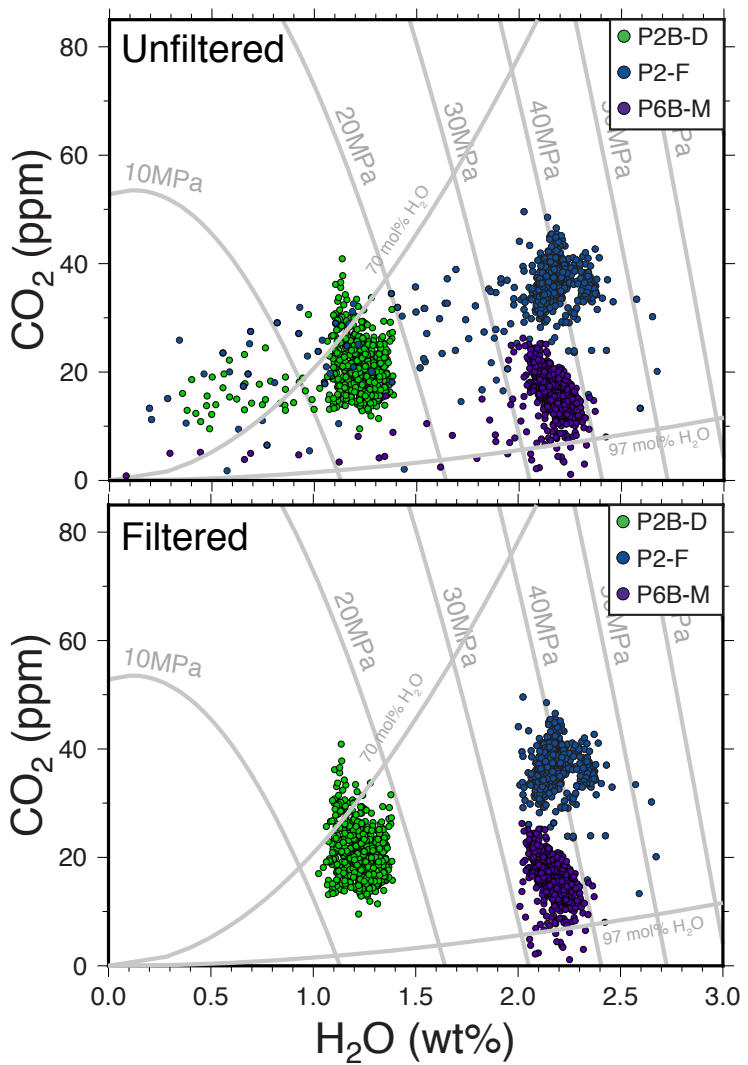


Figure DR6: Unfiltered and filtered versions of data presented in Figure 2 of the main text. For the filtered data set, regions of samples P2B-D, P2-F and P6B-M with poor spectra or sample wedging have been removed (see Fig. DR4).

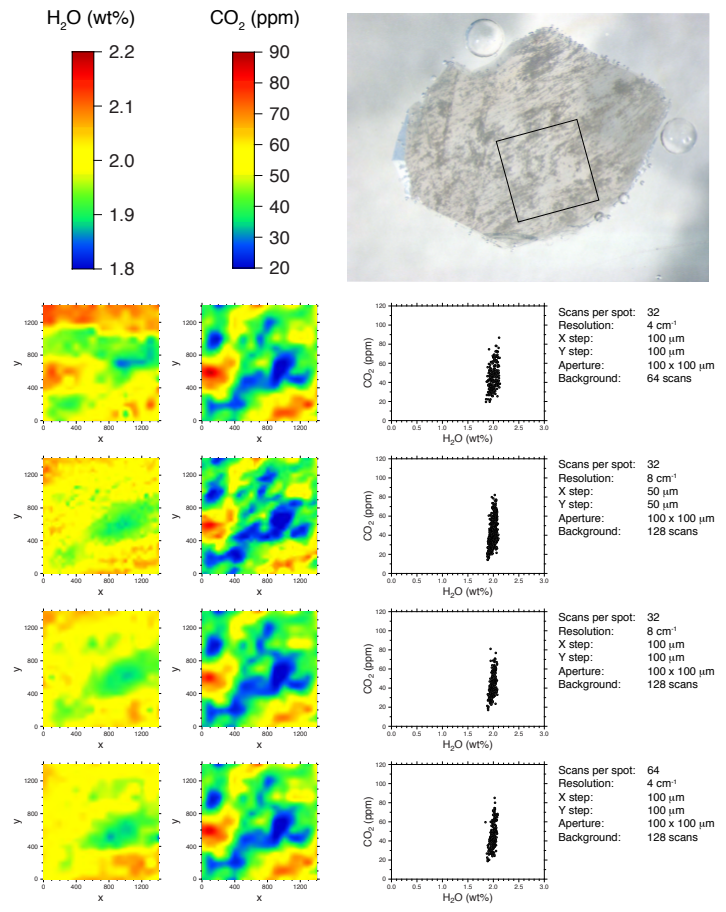


Figure DR7: Sensitivity of CO₂ and H₂O concentration maps to analytical parameters such as aperture size, spectral resolution, number of scans, and step spacing.

DR2 Cooling rates

We calculate the cooling rate undergone by each clast using the hydrous species speedometer of Zhang et al. (2000) (Fig. DR8). Six of the eight clasts yield cooling rates that are consistent with an air quench during the eruption. The other two clasts yield cooling rates that are two or more orders of magnitude slower, suggesting that they may have cooled below the glass transition within the magma feeder system. One of these clasts (sample P10-I), exhibits a range in cooling rates of five orders of magnitude, which is unrealistic given that the clast is centimeter-sized. This sample should be disregarded because the large scatter is due to analytical uncertainty in the concentration of molecular water (H_2O_m) at low total water contents.

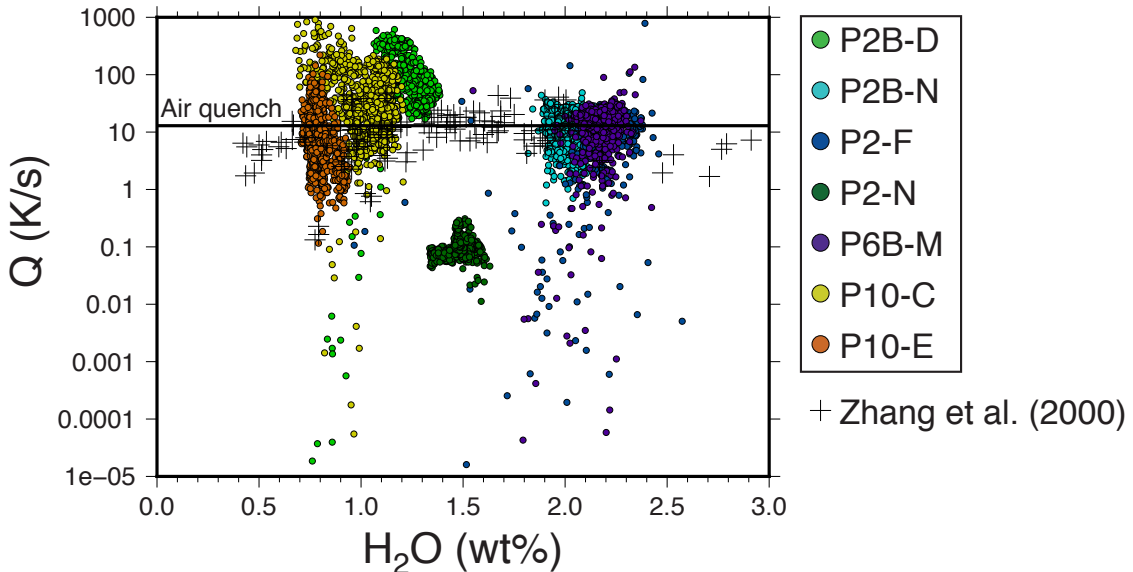


Figure DR8: Cooling rates of obsidian pyroclasts. Most clasts cluster around 10K/s, which is consistent with rapid cooling during air fall. The scatter in the data is attributable to noise in the H_2O_m peak at 5230 cm^{-1} , which increases with decreasing total water content. Sample P10-I (0.5 wt% H_2O) is not shown because the H_2O_m peak is too noisy at low total water to retrieve accurate cooling rates.

DR3 Diffusion modeling

For the diffusion modeling, we use samples P10I and P2N because the volatile concentration gradients in the y- and z-dimensions can justifiably be neglected. For diffusive homogenization in one dimension, we have:

$$\frac{\partial C_i}{\partial t} = D_i \frac{\partial^2 C_i}{\partial x^2} + \frac{\partial D_i}{\partial x} \frac{\partial C_i}{\partial x}, \quad (\text{DR2})$$

where i refers to either CO_2 or H_2O , and D_i is the diffusivity. The diffusivities of both H_2O and CO_2 depend on T , P and water content (Zhang and Behrens, 2000; Zhang et al., 2007). Check: For $T = 800^\circ\text{C}$, $P = 20\text{ MPa}$, and $\text{H}_2\text{O}_t = 1.5\text{ wt}$, $D_{\text{H}_2\text{O}_t} = 2.48\text{ }\mu\text{m}^2/\text{s}$ and $D_{\text{CO}_2} = 0.47\text{ }\mu\text{m}^2/\text{s}$. Since we

lack knowledge of the thermal history experienced by the clasts, we assume a constant temperature of 800°C and a pressure that is appropriate for each sample (Fig. 1B). For the model results shown in Fig. 3, the initial conditions are step functions in the concentrations of CO₂ and H₂O distributed throughout the model domain. By necessity, we neglect the influence of volatile gradients that are outside of the model domain and assume fixed concentration boundary conditions. Despite these simplifications, the model can reproduce the observed gradients in subdomains of the clasts and can be used to place constraints on the longevity of intraclast heterogeneities.

References

- Behrens, H., Tamic, N., Holtz, F., 2004. Determination of the molar absorption coefficient for the infrared absorption band of CO₂ in rhyolitic glasses. *American Mineralogist* 89 (2-3), 301–306.
- Newman, S., Stolper, E. M., Epstein, S., 1986. Measurement of water in rhyolitic glasses - calibration of an infrared spectroscopic technique. *American Mineralogist* 71 (11), 1527–41.
- Rust, A., Cashman, K., Wallace, P., 2004. Magma degassing buffered by vapor flow through brecciated conduit margins. *Geology* 32 (4), 349–352.
- von Aulock, F. W., Kennedy, B. M., Schipper, C. I., Castro, J., Martin, D., Oze, C., Watkins, J. M., Wallace, P. J., Puskar, L., Bégué, F., et al., 2014. Advances in Fourier transform infrared spectroscopy of natural glasses: From sample preparation to data analysis. *Lithos* 206, 52–64.
- Wessel, P., Smith, W., J. S., F, W., 2013. Generic mapping tools: Improved version released. *EOS Trans. AGU* 94 (45), 409–410.
- Zhang, Y., Behrens, H., 2000. H₂O diffusion in rhyolitic melts and glasses. *Chemical Geology* 169 (1), 243–262.
- Zhang, Y., Belcher, R., Ihinger, P., Wang, L., Xu, Z., Newman, S., 1997. New calibration of infrared measurement of dissolved water in rhyolitic glasses. *Geochimica et Cosmochimica Acta* 61 (15), 3089–3100.
- Zhang, Y., Xu, Z., Behrens, H., 2000. Hydrous species geospeedometer in rhyolite: Improved calibration and application. *Geochimica et Cosmochimica Acta* 64 (19), 3347–3355.
- Zhang, Y., Xu, Z., Zhu, M., Wang, H., 2007. Silicate melt properties and volcanic eruptions. *Reviews of Geophysics* 45 (4).